Steel and Composite Structures, *Vol. 23, No. 1 (2017) 17-29*
DOI: https://doi.org/10.12989/scs.2017.23.1.017

Experimental and analytical performance evaluation of steel beam to concrete-encased composite column with unsymmetrical steel section joints

Yunfeng Xiao, Lei Zeng *, Zhenkun Cui, Siqian Jin and Yiguang Chen

School of Urban Construction, Yangtze University, Jingzhou, 434023, China

(Received February 13, 2016, Revised December 01, 2016, Accepted December 06, 2016)

Abstract. The seismic performance of steel beam to concrete-encased composite column with unsymmetrical steel section joints is investigated and reported within this paper. Experimental and analytical evaluation were conducted on a total of 8 specimens with T-shaped and L-shaped steel section under lateral cyclic loading and axial compression. The test parameters included concrete strength, stirrup ratio and axial compression ratio. The response of the specimens was presented in terms of their hysterisis loop behavior, stress distribution, joint shear strength, and performance degradation. The experiment indicated good structural behavior and good seismic performance. In addition, a three-dimensional nonlinear finite-element analysis simulating was conducted to simulate their seismic behaviors. The finite-element analysis incorporated both bond-slip relationship and crack interface interaction between steel and concrete. The results were also compared with the test data, and the analytical prediction of joint shear strength was satisfactory for both joints with T-shaped and L-shaped steel section columns. The steel beam to concrete-encased composite column with unsymmetrical steel section joints can develop stable hysteretic response and large energy absorption capacity by providing enough stirrups and decreased spacing of transverse ties in column.

Keywords: concrete-encased structure; unsymmetrical; seismic behavior; numerical analysis

1. Introduction

The concrete-encased composite structure, as typical composite structure with high capacity and good seismic performance (Xu *et al*. 2015), has been extensively adopted in super high-rise buildings. In order to satisfy the structure of plane layout and uneven force state in practical engineering, concrete-encased composite columns with T-shaped section and L-shaped section are often adopted for the edge and corner columns.

Extensive researches have been completed for seismic performance of reinforced concrete structures. Experimental investigation was executed by Zhang *et al*. (2013) to study the aseismic performance of fabricated concrete T-shape exterior RC joint. It was observed that the failure processes of the joints with two forms were basically the same. Assembled joint has good integrity and deformation ability. RC column-beam joints damaged by simulated earthquake were studied by Yu *et al*. (2010), including pre-damage, rehabilitation and re-test under reverse cyclic loading. Study mainly concentrated on the effect of different strengthening schemes and different levels of pre-damage. Specimens which were rehabilitated performed the same seismic capacity as before. Meanwhile, Metelli *et al*. (2015) attempted to design a model for external beam–column joints of existing RC frame. Joint shear behavior and bond slip components were considered. Modified Softened Strut-accurately calculate the seismic performance of the joint. Moreover, numerical simulation was also carried out by Constanze *et al*. (2015) to evaluate the effect of steel fiber reinforced concrete (SFRC). Under the influence of adding fibers, residual tensile strength was significant improved.

Furthermore, symmetrical concrete-encased composite structures have been fully studied which includes seismic performance of corresponding joints and frames (Zheng and Zeng 2008, Zeng *et al*. 2015a). Xue *et al*. (2011) brought out bearing capacity of concrete-encased steel specially-shaped column-beam joint. Strains of stirrups, horizontal web members, steel web and the shear mechanism were particularly analyzed. The formulas of shear and torsion bearing capacity had been given. Concrete-encased steel with high strength and high performance concrete was taken into consideration by Zheng and Zeng (2008). In addition, Chen *et al*. (2014) developed a new type of joint, which was made of concrete-filled steel tubular (CFST) column and a RC beam. It was concluded that specimens nearly failed in the CFST column region. The innovative connection had the advantage of good axial compressive strength and energy dissipation capacity. Recently, a shear wave based active sensing approach was proposed to research on the bond-slip behavior in the concrete-encased composite structure (Zeng *et al*. 2015b). The post-collapse behavior of concrete encased steel composite columns under axial compression was studied, and a numerical method considered fiber element discretization was proposed (Ky *et al*. 2015). In general, a lot of summaries have been carried out simul-taneously, and the mature design theories have been formed. The results showed that this type of structure has high bearing capacity and good seismic performance.

∗Corresponding author, Professor
E-mail: zenglei@yangtzeu.edu.cn

http://www.techno-press.org/?journal=scs&subpage=6
ISSN: 1229-9367 (Print), 1598-6233 (Online)

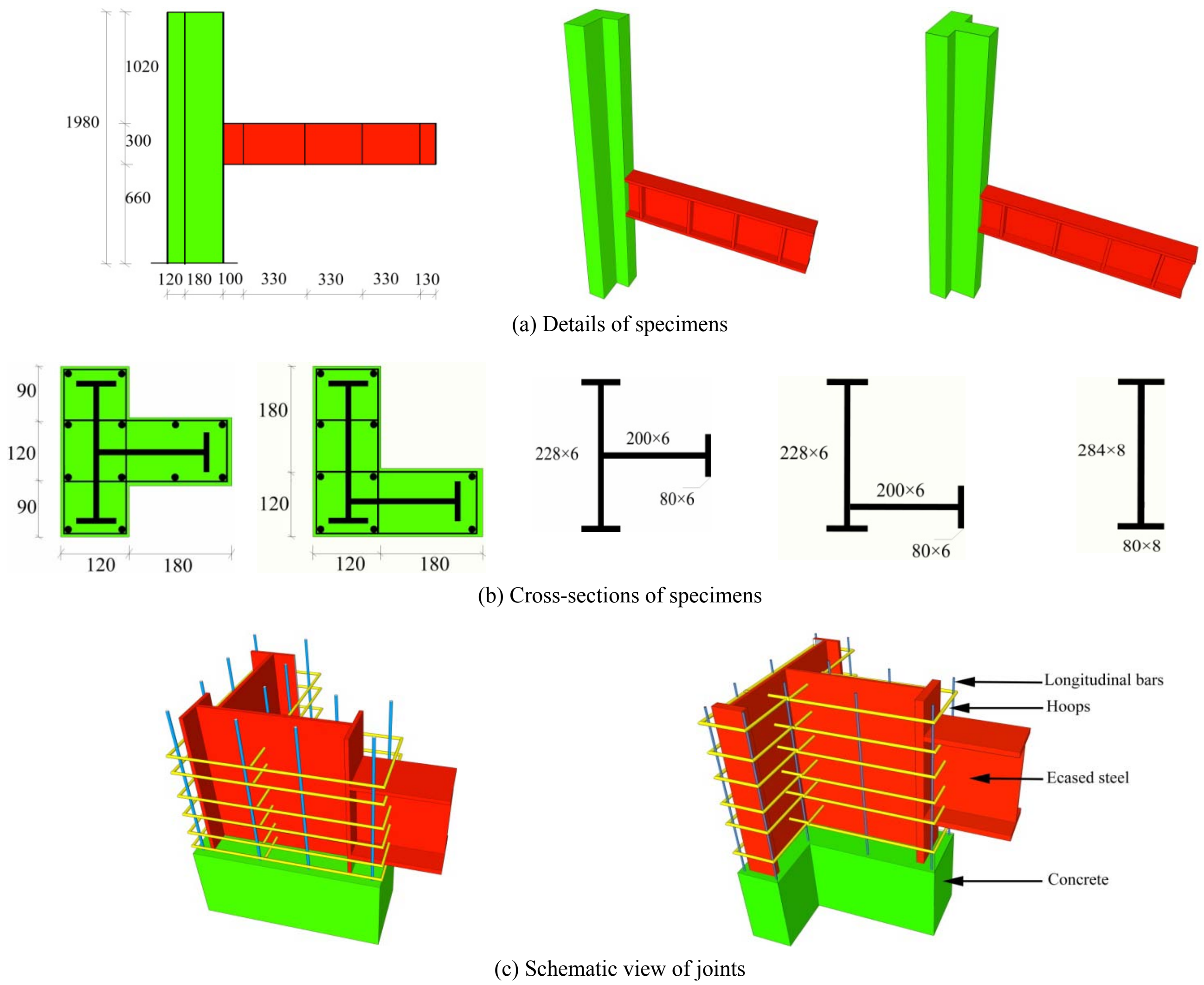

Fig. 1 Specimen dimension and steel details

However, current researches on concrete-encased composite column with unsymmetrical steel section joints have not yet been systematically achieved. Present achievements are mainly on the joints between reinforced concrete beams and columns (Zhou *et al*. 2015). The corresponding design formulas and construction measures are not established in present Chinese code (Central Research Institute of Building and Construction 2006, China Academy of Building Research 2010a). Joint as the most complex part in the frame structure has assumed a huge load of earthquake. Properties under the effect of earthquake and the corresponding design strategies nowadays become a focus in unsymmetrical concrete-encased composite structures investigation.

As a consequence, in order to evaluate the seismic performance of steel beam to concrete-encased composite column with unsymmetrical steel section joints, reversed cyclic loading was applied on 4 joints with T-shaped section and 4 joints with L-shaped section in the present study. Experimental investigations had been carefully carried out on the effect of a variety of parameters as concrete strength, volumetric transverse reinforcing ratio and axial compression ratio. Two failure modes including shear diagonal compression failure and core zone welding crack failure were observed. The results showed that this kind of structure performs good ductility and energy dissipation capacity according to relevant phenomena and data obtaining from test. Furthermore, finite element analysis has been executed basing on analytical model by ANSYS. Both bond-slip relationship and crack interface interaction in the normal, longitudinal and transverse directions were considered. The hysteretic curves and envelope curves of FEA were obtained. It is also observed that calculation results are fairly accurate, and agree well with verification results. Parametric studies on seismic behavior were accomplished and the simulation results indicated that by increasing of axial compression ratio or concrete strength, bearing capacity increased though ductility reduced contrarily.

2. Experimental program

2.1 Details of specimens

8 specimens were designed and detailed by the desired scenario of “strong column-weak beam” and “strong joint-

Table 1 Parameters of specimens

Specimen	Concrete strength grade	Volumetric stirrup ratio ρ_v%	Axial compression ratio n
TJ-1	C30	0.825	0.3
TJ-2	C30	0.825	0.6
TJ-3	C30	1.651	0.3
TJ-4	C60	0.825	0.6
LJ-1	C30	0.825	0.3
LJ-2	C30	0.825	0.6
LJ-3	C30	1.651	0.3
LJ-4	C60	0.825	0.6

Table 2 Materials properties of steel

Material	Thickness/ Diameter (mm)	Yielding strength f_y /MPa	Ultimate strength f_u /MPa	Elastic modulus E_s /MPa
Reinforcement	Φ^b4	435.4	513.1	2.1×10^5
	Φ10	305.3	404.2	2.1×10^5
Encased steel	6 mm	324.1	437.5	2.0×10^5
	8 mm	272.2	410.6	2.0×10^5

Table 3 Materials properties of concrete

Concrete strength grade	Cubic compressive strength f_{cu} /MPa	Axial compressive strength f_c /MPa	Elastic modulus E_c /MPa
C30	40.25	25.67	3.0×10^4
C60	62.80	41.68	3.6×10^4

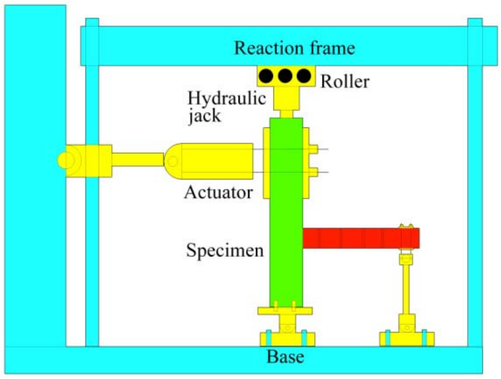

Fig. 2 Test setup

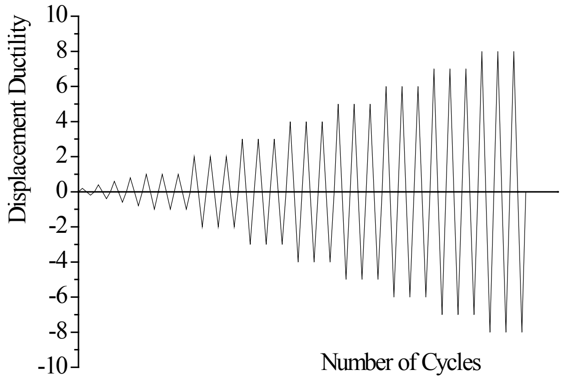

Fig. 3 Loading history

weak member". All the specimens have the same dimensions and cross-sections as presented in Fig. 1. The related parameters including concrete strength, volumetric stirrup ratio (ρ_v) and axial compression ratio (n) were taken into consideration for specific experimental observation. n and ρ_v are given by Eqs. (1) and (2)

$$n = N / f_c A \tag{1}$$

where N is the axial load applied; A is the area of cross-section; f_c is concrete axial compressive strength.

$$\rho_v = \sum n_i A_{si} l_i / A_{cor} s \tag{2}$$

where n and l are quantity and length of stirrups; A_{si} is area of stirrup section; A_{cor} is area of concrete in core region; s is the space of stirrup.

The parameters of specimens are showed in Table 1. Each specimen has twelve 10 mm-diameter longitudinal bars. Deformation bars with 8 mm in diameter are used as hoop reinforcement. Encased steel is designed with L-shaped and T-shaped hot-rolled structural steel at grade of Q235. Result from material test particularly determines the average values of mechanical properties as shown in Tables 2 and 3.

2.2 Test setup and procedure

The test was executed in Civil Engineering Experiment Center of Yangtze University. Specimens were subjected to a lateral cyclic loading to simulate earthquake load in addition to a constant axial load. The schematic loading system is showed in Fig. 2. The constant axial load was exerted to the column top and maintained stably by the hydraulic jacks. The roller system was installed under the reaction frame, transferring the axial load and releasing lateral displacements. Foundation of the column and end of beam were restrained by hinge supports.

Displacement control method was applicable to obtain critical phenomenon throughout the procedure as presented in Fig. 3. The defined yield displacement Δ_y was characterized by the tip displacement corresponding to yielding of column top. In the beginning one cycle was employed at each displacement level, while subsequently turned to three cycles once Δ_y had been attained. Test was finished until the load down to 85% of ultimate lateral load or the specimen was unable to continue bearing axial force (Shafaei *et al.* 2014).

Figs. 4 and 5 exhibit the layout of displacement transducers and strain measurements. D1 and D2 were placed in joint to measure the shear deformation in core region. D3 and D4 were placed in beam end to measure the

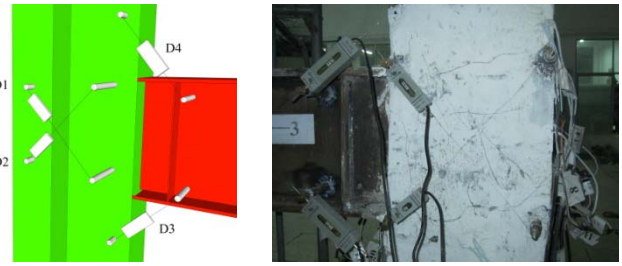

Fig. 4 Layout of displacement transducers

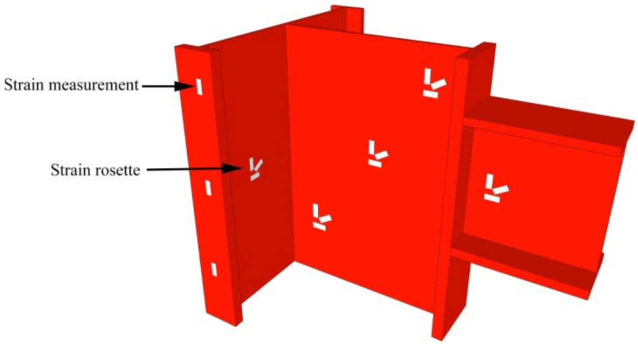

Fig. 5 Steel and reinforcement strain measurement

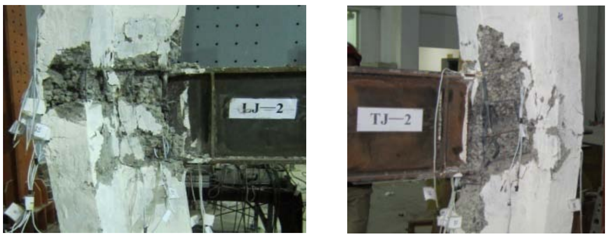

(a) Shear diagonal compression failure

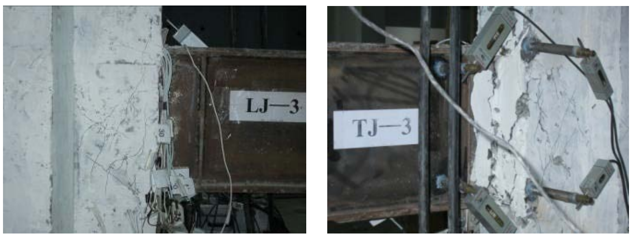

(b) Core zone welding crack failure

Fig. 6 Failure modes of specimens

corresponding displacement. In addition, displacement transducers in column base and beam top were used to measure the relative rotation. Strain rosettes were installed on the steel skeleton in joint region.

2.3 Failure mode

Under the effect of constant axial load and reverse cyclic load, specimens mainly had two failure modes: (a) shear diagonal compression failure; (b) core zone welding crack failure as illustrated in Fig. 6.

Mode (a) mainly had the characteristic of drastic damage in joint, and was clearly observed in LJ-2 and TJ-2. Oblique cracks firstly appeared in joint region, and then turned to plenty of X-shaped cracks. Core concrete had a phenomenon of massive spalling and crushing with the cracks having developed into deeper and wider. Longitudinal bars were yielded and protruded while hoop reinforcements were completely fractured. Stiffening ribs were practically separated from steel skeleton. This mode mostly occurred in the specimens with high axial compression ratio (n = 0.6). Concrete and steel were fully utilized, demonstrating satisfactory seismic performance.

Mode (b) mainly had the characteristic of welding abruption in core region, and was clearly observed in LJ-3and TJ-3. Cracks came out in intersection of beam flange and column and eventually formed crossing cracks. Local concrete was crushed under the flange. Longitudinal bars and stirrups had not reached the yield strain. A noise was obviously heard, indicating welding crack failure and obvious degeneration of hearing capacity and stiffness. This mode mostly occurred in the specimens with low axial compression ratio (n = 0.3).

3. Finite element analysis

3.1 General descriptions

In this section, the commercial finite element software ANSYS is used to simulate the specimens. According to the validation with reliable conclusions, some relevant parametric studies are managed under the finite element model (FEM). Specimens investigated in this study should be modeled in four main components, comprising encased steel, concrete, reinforcing bars and the bond-slip part. Encased steel and concrete are modeled using “SOLID” element available in the ANSYS element library. Reinforcing bars are modeled with “LINK” element encased by concrete, whereas the stirrups are enclosed connecting the main reinforcement. Bonding performance of steel skeleton and concrete is slightly poor and is modeled using “COMBINE” element (Zeng *et al*. 2010).

3.2 Geometric modeling

Correct finite element methods of the material characters are important for the completeness, validity and accuracy of results. The model dimension is strictly corresponding to the specimen. Longitudinal bars are covered by solid elements in a certain thickness, sharing one node with stirrup units in the intersection. Between the contact surface of concrete and steel there is a very small gap where the combine elements are inserted.

Reasonable selection of material element and moderate grid size in ANSYS are the key to obtained effective numerical analysis (Zeng *et al*. 2011). In connection region, different size specifications of macro-elements were meshed with 6 mm and 8 mm size, the remaining part was meshed with 50 mm size elements.

In addition, column foundation and the end of beam are hinged in three displacements degrees of freedom, however rotational degrees of freedom are released (Pantelides *et al*. 2008, Kovács *et al*. 2008). On the basis of ANSYS program, the pressure is designed as uniform loads on the surface (Vasdravellis *et al*. 2009, Cheng *et al*. 2003). For higher numerical accuracy, displacements were performed in small loading step, which has characteristics of time-dependent correlation. Convergence of computation in different displacement growth rate seriously affects the calculation process, therefore initial loading procedure conducts increment of 1 mm through synthetic analysis.

3.3 Material modeling of steel

The steel skeleton and beam units are simulated with SOLID45 element, which is 3D entity unit with 8 nodes (Wang and Li 2011). Each node has three degrees of freedom as shown in Fig. 7(a). This element type can degenerate as pentahedral prism or tetrahedral element. Unit input data includes eight nodes and normal anisotropic material properties, which is defined in coordinate system. And secondly, the reinforcing bars are simulated with plane element LINK8 to bear tension and pressure as inseparate truss in the form of bar units.

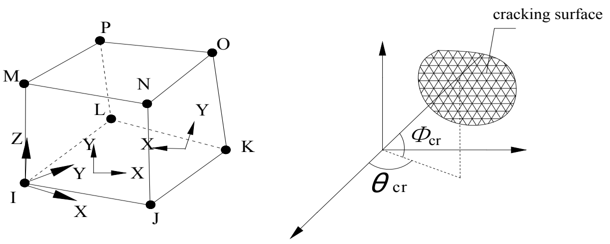

(a) Solid45 (b) Cracking surface in solid65

Fig. 7 Solid element

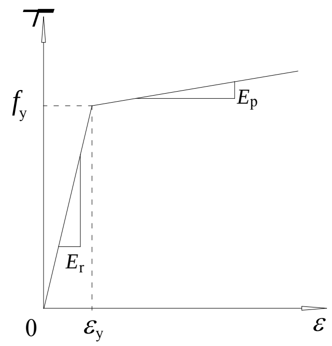

Fig. 8 Stress-strain relationship of steel

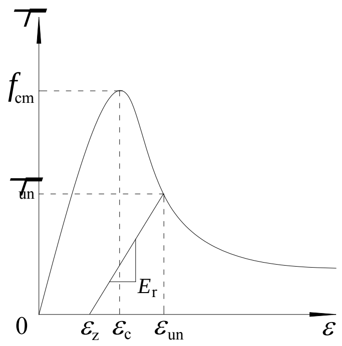

Fig. 9 Stress-strain relationship of concrete under repeated loading

The specific nonlinear stress–strain curve (China Academy of Building Research 2010b) of material is allowed in ANSYS as shown in Fig. 8. Model of bilinear kinematic (BKIN) is adopted in plasticity analysis. Steel and reinforcing bars obey the Von Mises yield criterion. Also the criterion of non-linear kinematic hardening and related flowing criterion are taken into account to achieve real simulation of material properties.

$$\sigma_s = \begin{cases} E_r \varepsilon_s & \varepsilon_s \le \varepsilon_y \\ f_y + 0.01(\varepsilon_s - \varepsilon_y) & \varepsilon_s > \varepsilon_y \end{cases} \tag{3}$$

Where E_r is elastic modulus of steel, E_p is modulus in plastic stage, σ_s is stress of steel skeleton and reinforcing bars, ε_s is strian of steel skeleton and reinforcing bars, f_y is yield strength of steel, ε_y is strain corresponding to the yield strength.

3.4 Material modeling of concrete

Concrete has complex mixture of properties, which is considered as isotropic property in initial stage and anisotropic property when cracking. Concrete is simulated with SOLID65 element, which has the function of tension cracking and crushing as shown in Fig. 7(b). The idealized stress–strain curve for the concrete has great influence on the nonlinear analysis as shown in Fig. 9. In order to accurately describe the isotropic and anisotropic material properties in different stages (Enrico and Sherif 2004), model of multi linear kinematic hardening (MKIN) is appliable to simulation. Mechanical characteristics of cracking and crushing, uniform hardening criterion, related flowing criterion and William-warnker five parameters failure criterion are taken into consideration.

$$\sigma = E_r(\varepsilon - \varepsilon_z) \tag{4}$$

$$E_r = \frac{\sigma_{un}}{\varepsilon_{un} - \varepsilon_z} \tag{5}$$

$$\varepsilon_z = \varepsilon_{un} - \left(\frac{(\varepsilon_{un} + \varepsilon_{ca})\sigma_{un}}{\sigma_{un} + E_c \varepsilon_{ca}} \right) \tag{6}$$

$$\varepsilon_{ca} = \max\left(\frac{\varepsilon_c}{\varepsilon_c + \varepsilon_{un}}, \frac{0.09\varepsilon_{un}}{\varepsilon_c} \right) \sqrt{\varepsilon_c \varepsilon_{un}} \tag{7}$$

Where σ is compressive stress of concrete, ε is corresponding strain of σ, ε_z is residual strain when concrete is unloaded to zero stress, E_r is deformation modulus of unloading and reloading, ε_{un} and σ_{un} are respective stress and strain of beginning to unload in skeleton curve, ε_{ca} is additional strain, f_{cm} is concrete compressive peak, ε_c is corresponding strain of f_{cm}.

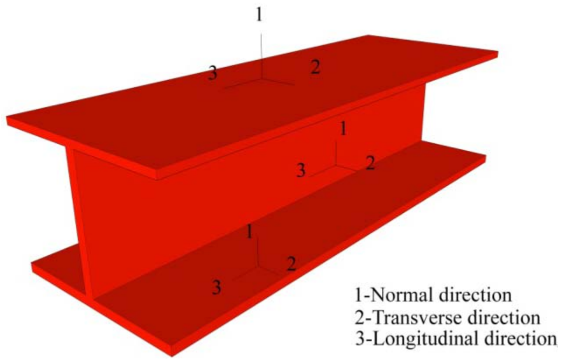

Fig. 10 Directions of spring elements

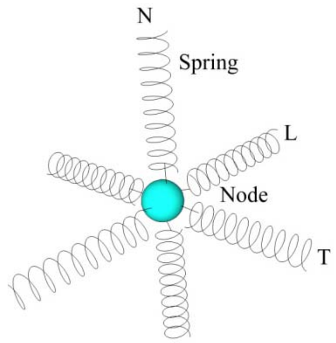

Fig. 11 Spring in local coordinate system

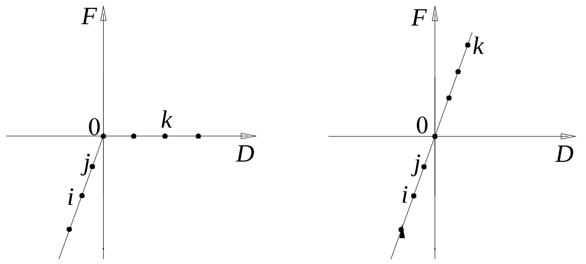

(a) Normal direction (b) Transverse direction

Fig. 12 *F-D* curve

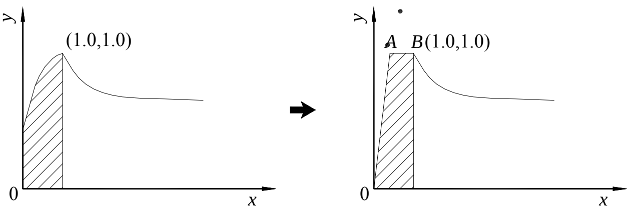

Fig. 13 Modified *τ-s* standard curve

3.5 Constitutive law of bond-slip

The bond slip between steel and concrete has a very significant effect on the bearing capacity of joints. Spring elements with zero length are set up in three directions as shown in Figs. 10 and 11, including the normal direction (which is vertical to the connection surface between steel and concrete), longitudinal direction (which is parallel to the length direction and vertical to the connection surface) and transverse direction (which is vertical to the length direction and parallel to the connection surface).

In normal direction, deformation in concrete-encased composite column is relatively small when getting bond failure. Therefore, the interaction is simplified as spring with high stiffness coefficient approximating to the concrete elastic modulus. These behaviors can be described using *F-D* curve which is broken line with high slope in the third quadrant but zero in the first quadrant. It is characterized by simulation which does not transfer tensile stress as shown in Fig. 12(a).

In transverse direction, stirrups and steel have a strong constraint effect on the core concrete. The relative displacement of steel and concrete in this direction is small and can be neglected. Therefore, the stiffness coefficient of *F-D* curve is taken as a large constant value approximating to concrete shear modulus. The curve is a straight line which passes through the origin with high slope as shown in Fig. 12(b).

In longitudinal direction, stiffness coefficient has high nonlinearity (Abbas *et al*. 2014), which is need to be described through the *τ-s* curve as shown in Fig. 13. Bond stress of the spring as the relationship above is calculated by Eq. (8) and the *F-D* curve of the nonlinear spring elements is calculated by Eq. (9).

$$\tau = \tau(s, x_i) \tag{8}$$

$$F = \tau(D, x_i) \cdot A_i \tag{9}$$

Where A_i is the corresponding area of the spring in the connection surface; τ and s are bond stress and the corresponding slip deformation respectively; F and D are shear and translational displacement respectively.

According to the location, the springs are divided into three situations, which are intermediate nodes, edge nodes

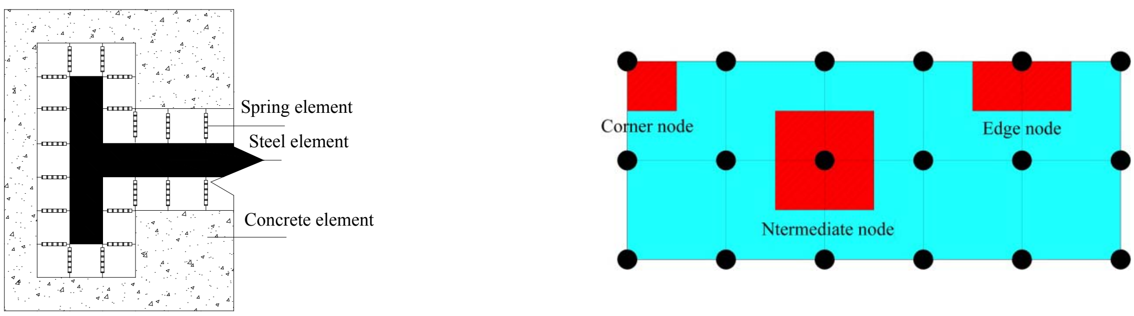

Fig. 14 Area distribution of bond element

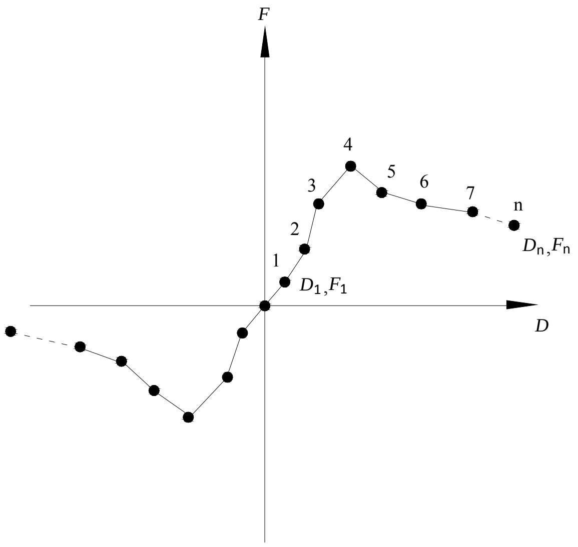

Fig. 15 *F-D* curve in ANSYS program

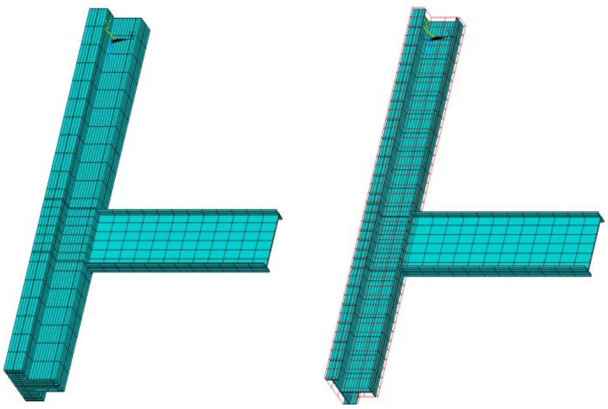

(a) Model of T-shaped steel section

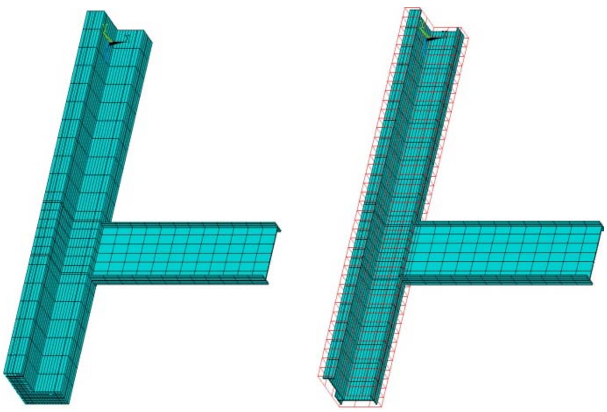

(b) Model of L-shaped steel section

Fig. 16 FEA models

and corner nodes. Each node occupies a quarter of its adjacent bond area. The specific rules of the division are shown in Fig. 14. To input bond-slip constitution for bond element in FEA, the *F-D* curve is calculated according to experimental data measured by Li *et al*. (2010).

ANSYS program requires that the curve must go through the origin. So certain amendments of standard τ-s curve are made to satisfy the requirements of the calculation basing on the bond energy equivalent principle. When defining *F-D* curve as shown in Fig. 15, deformation must be increased from the third quadrant (compressed region) to the first quadrant (tensile region). Each point has its own slope, which can be positive or negative, but the slope through the origin must be positive.

Fig. 16 shows that the accurate models with T-shaped section and L-shaped section. The steel skeleton and reinforcing bars are obviously exposed. In joint region, denser grids are meshed to obtain complete analysis. However nonessential part is roughly meshed in order to simplify the calculation.

4. Comparison between experimental investigations and FEA

4.1 Strains and stress

The strain measurement included steel skeleton strain, stirrup hoop strain and steel flange box strain. Because of the similarity in strain distributions, TJ-2 was taken as an example. Principal strain and direction of steel web in each phase is shown in Fig. 17. It showed that most of the steel web yielded when getting yield stage, and the direction varied from 28° to 34°. Steel web mainly sustained shear when getting failure stage, and the direction was about 45°. Furthermore the value of principal compressive strain was always smaller than that of tensile strain.

In initial stage, stirrup hoop strain was small and varied from 250 $\mu\varepsilon$ to 300 $\mu\varepsilon$. It indicated that both steel and concrete in core region mainly bore the shear. In yield stage, strain varied from 1570 $\mu\varepsilon$ to 1670 $\mu\varepsilon$ and stirrup hoops practically yielded. In failure stage, strain suddenly increased and basically varied from 2450 $\mu\varepsilon$ to 2600 $\mu\varepsilon$.

Strain of steel flange box varied from 200 $\mu\varepsilon$ to 350 $\mu\varepsilon$ which is in a cyclic situation of compression and tension. It had the function of transferring internal force and confining concrete, but had little effect for resisting shear. In failure stage, Steel flange box had welding crack failure and strain varied from 1350 $\mu\varepsilon$ to 1500 $\mu\varepsilon$.

As is presented in Fig. 18, The failure modes of finite element analysis (FEA) are obtained. The red areas that represent the maximum stress appeared in joint, which agrees well with that of the test.

4.2 Hysteretic curves

Hysteretic curves obtained from experimental investigations and FEA results are shown in Fig. 19. However the experiment of LJ-4 was abortive because of equipment

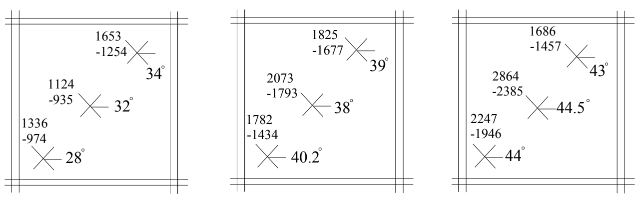

Fig. 17 Principal strain and direction of web steel

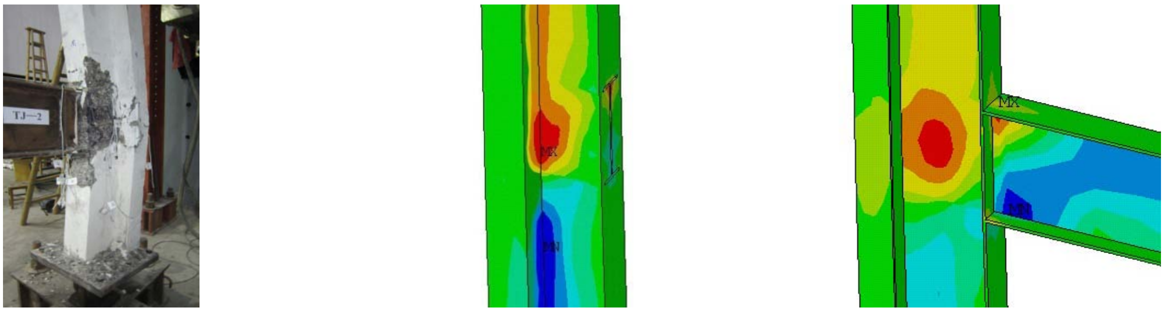

(a) Comparison of T-shaped steel section

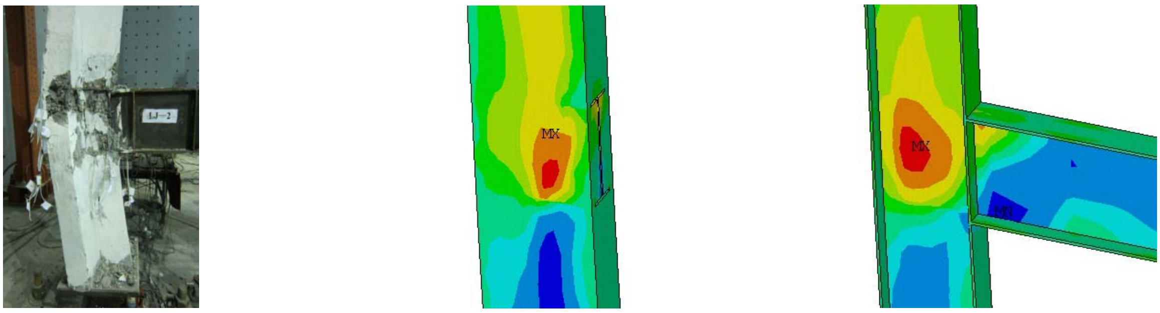

(b) Comparison of T-shaped steel section

Fig. 18 Comparisons of stress between finite element analysis and test results

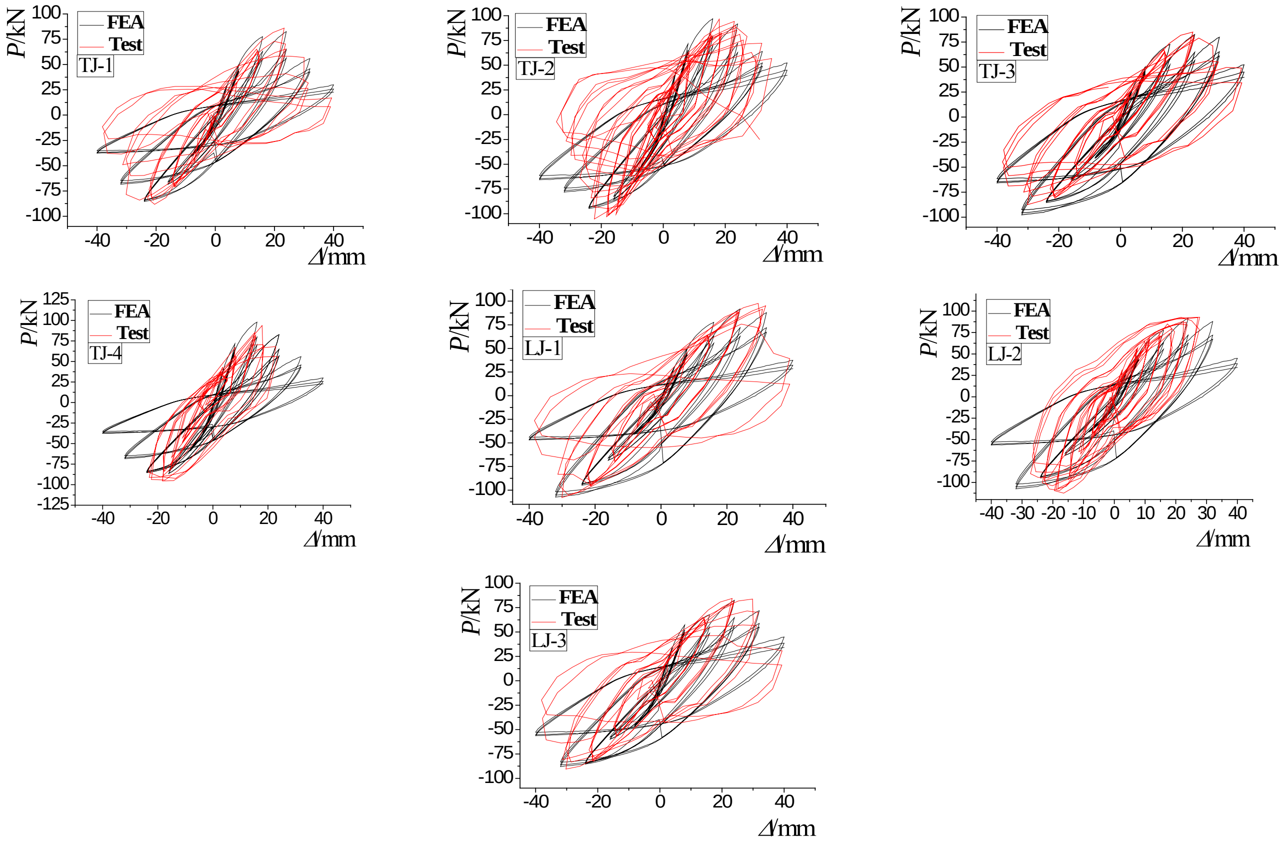

Fig. 19 Comparison of hysteretic curves between experimental and FEA results

fault. Hysteretic curves were always between shuttle-shaped and S-shaped. Specimens performed an initial elastic response and linear P-Δ relationship. Obvious degradation occurred in both positive and negative strength in each displacement level. Bond-slip performance, charac-terized by maximum strength reduction and stiffness degradation, firstly occurred in elastic-plastic stage. When displacement increased, pinching effects became signifi-cant, which was

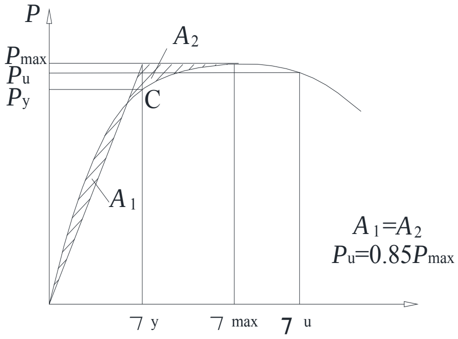

Fig. 20 Definitions of yield point and failure point

mainly due to closing and opening of concrete cracks. In the whole loading process specimens still maintained good structural behavior and seismic performance.

To simplify calculation process in the numerical studies, the load steps in program are subjected to one cycle before the yield displacement. Lateral cyclic loading is applied by small steps. Arc-length method and Newton–Raphson method are adopted for valid convergence. The contraction degree of hysteresis loops is similar to which of test results. Axial compression ratio has great influence on failure mode. It is illustrated that the numerical results truly reflect experimental investigations.

4.3 Envelope curves

Envelope curves are connected by peak values of first cycle at each lateral displacement level (Chidambaram and Agarwal 2015). Equivalent energy method is adopted to confirm the yield point and 85% of maximum load is taken as the damage point.

Envelope curves of TJ-2 and TJ-4 show that both initial stiffness and ultimate load are higher, but bearing capacity degenerates rapidly. Higher axial force produced greater effect on constraining the core concrete. In addition, the effect of diagonal strut was strengthened in the core region.

Envelope curves of TJ-1 and TJ-3 show that the effect on bearing capacity is unnoticeable with the improvement of stirrup ratio. Joint had been entirely destroyed before stirrups exerted effective function of constraint. So the effect of the stirrup ratio was not reflected in this experiment.

Envelope curves of TJ-3 and TJ-4 show that concrete strength has positive influence. Ultimate bearing capacity of TJ-4 is larger than that of TJ-3 under the same conditions, but the descending branch becomes steeper.

Fig. 21 indicates the comparison of skeleton curves between experimental investigations and FEA results. Each group has the same initial stiffness. The ultimate loads of FEA results agree well with that of test, and obvious downward phases indicate the degeneration of bearing capacity. Table 4 shows the accuracy of skeleton curves. The negative ultimate load is underestimated by maximum of 12%, whereas the positive ultimate load is identical. The maximum composite mean absolute error is 0.93%. However the simulation agrees well with the experimental results.

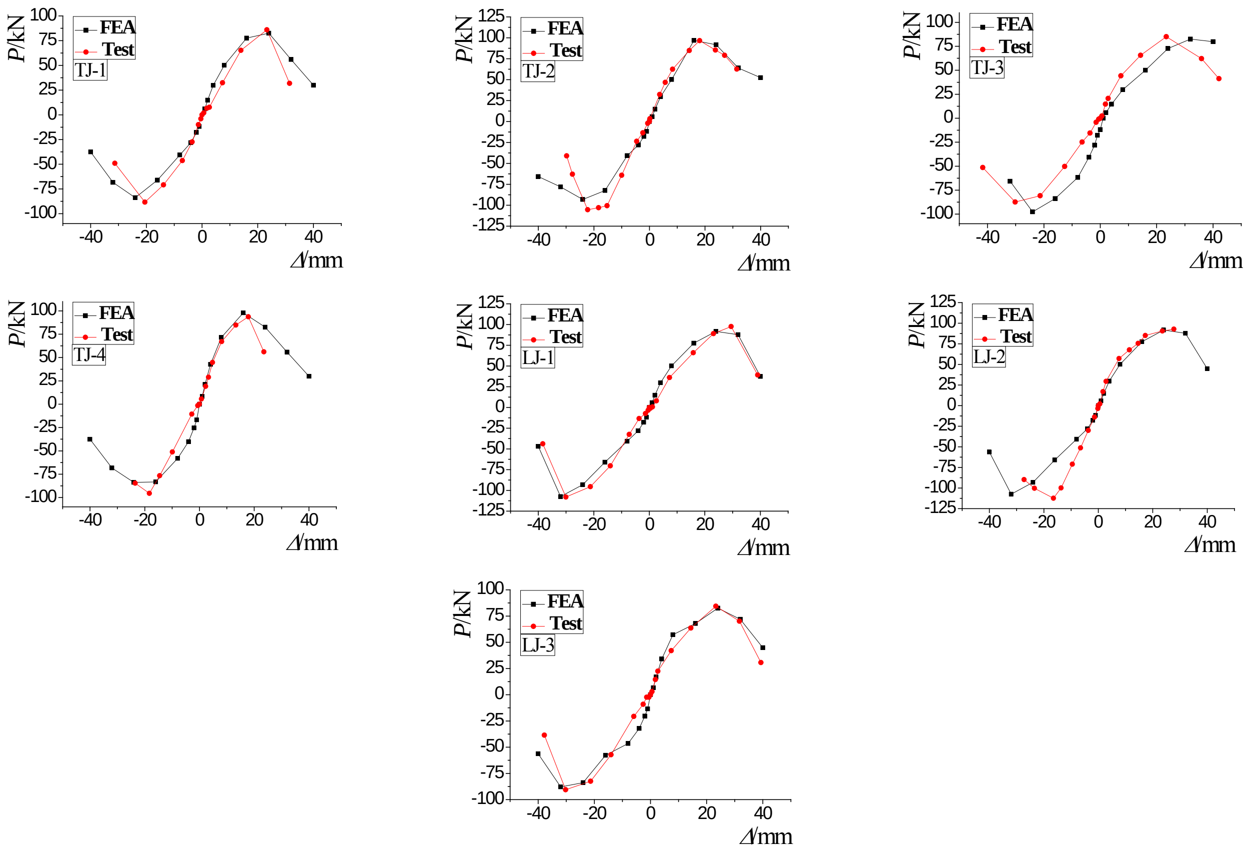

Fig. 21 Comparison of skeleton curves between experimental and FEA results

Table 4 Accuracy of skeleton curves between experimental and FEA results

Number of specimen	Ultimate load in text P_1 /kN		Ultimate load in FEA P_2 /kN		Mean absolute error
	Positive	Negative	Positive	Negative	
TJ-1	85.97	-88.24	82.58	-83.81	1.046
TJ-2	96.61	-105.39	91.76	-93.13	1.093
TJ-3	85.04	-87.43	82.58	-97.66	0.957
TJ-4	93.69	-95.49	97.94	-83.81	1.041
LJ-1	97.67	-107.97	91.76	-107.43	1.032
LJ-2	92.78	-112.41	96.06	-105.26	1.019
LJ-3	84.43	-90.56	82.58	-87.90	1.026

4.4 Ductility

Relevant parameters are shown in Table 4. The displacement ductility coefficient μ is calculated by Eq. (10) (Zhou *et al*. 2012).

$$\mu = \Delta_u / \Delta_y \tag{10}$$

Where Δ_u is the displacement at 85% of lateral load and Δ_y is the displacement corresponding to the first yielding.

Inter-story drift ϕ is calculated by Eq. (11).

$$\phi = \mathrm{arctg}\frac{\Delta}{L_1 + L_2} \tag{11}$$

Where Δ is horizontal displacement at column top, L_1 and L_2 are geometric lengths from joint centroid to column top and bottom. ϕ_y and ϕ_u in Table 4 are the drift at yielding and failure points, respectively.

Column-to-beam rotation θ is measured by displacement meters at 45° and is calculated by Eq. (12).

$$\theta = \arcsin\frac{\delta \sin 45^\circ}{S} \tag{12}$$

Where δ is oblique displacement. θ_u is the rotation at failure point. S is diagonal length.

Displacement ductility coefficients of specimens are all about 3.0. Inter-story drift is 1/249-1/173 at yielding point and 1/92-1/53 at failure point. Column-to-beam rotation in joint is 0.017-0.026. Although the failure occurred in core region, specimens still satisfied the limit value of inter-story drift under rare earthquake in Chinese code.

Influence of concrete strength, stirrup ratio and axial compression ratio are observed clearly. With the increase of concrete strength and axial compression ratio, specimens have certain ductility degeneration. Comparing with TJ-1 and TJ-2, as axial compression ratio augments from 0.3 to 0.6, ductility degenerates for about 12.5%. Comparing with TJ-2 and TJ-4, as concrete strength increases from C30 to C60, ductility degenerates for about 14%. However with the increase of stirrup ratio, ductility is improved. It is mainly because that concrete is steadily in triaxial compression owing to constraint of stirrups. In summary, steel beam to concrete-encased composite column with unsymmetrical steel section joints perform good seismic behavior.

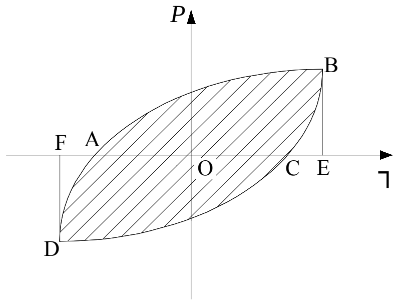

Fig. 22 Hysteretic loop and energy dissipation capacity

Table 5 Displacement ductility coefficient, inter-story drift, column-to-beam rotation and energy dissipation of specimens

Number of specimen		TJ-1	TJ-2	TJ-3	TJ-4	LJ-1	LJ-2	LJ-3
μ	Positive	3.16	2.71	3.49	2.86	3.15	-	3.16
	Negative	3.24	2.9	3.28	3.02	2.93	2.77	3.24
ϕ_y /rad	Positive	1/223	1/213	1/211	1/249	1/176	-	1/215
	Negative	1/238	1/232	1/174	1/231	1/163	1/217	1/173
ϕ_u /rad	Positive	1/71	1/75	1/60	1/92	1/56	-	1/63
	Negative	1/73	1/77	1/53	1/80	1/55	1/78	1/55
θ_u /rad		0.021	0.021	0.026	0.017	0.021	0.017	0.022
h_e		0.208	0.211	0.202	0.234	0.191	0.268	0.22

4.5 Energy dissipation

Equivalent viscous coefficient h_e is employed to reflect energy absorption capacity (Choi *et al*. 2010), which is calculated by Eq. (13).

$$h_e = \frac{1}{2\pi}\cdot\frac{S_{(\Delta ABC+\Delta CDA)}}{S_{(\Delta OBE+\Delta ODF)}} \tag{13}$$

Where $S_{(\Delta ABC+\Delta CDA)}$ is area of one hysteretic loop as illustrated in Fig. 22, and $S_{(\Delta OBE+\Delta ODF)}$ is the total area of triangle OBE and triangle ODF according to the points of maximum horizontal load and maximum horizontal displacement.

In general the equivalent viscous coefficients of reinforced concrete columns in bending failure vary from 0.1 to 0.2. The coefficients in Table 5 are all more than 0.191, and the maximum value reaches 0.268. It illustrates that steel beam to concrete-encased composite column with unsymmetrical steel section joints exhibit favourable energy absorption capacity.

4.6 Stiffness degradation

Stiffness K_i can be calculated by Eq. (14).

$$K_i = \frac{|+P_1| + |-P_1|}{|+\Delta_1| + |-\Delta_1|} \tag{14}$$

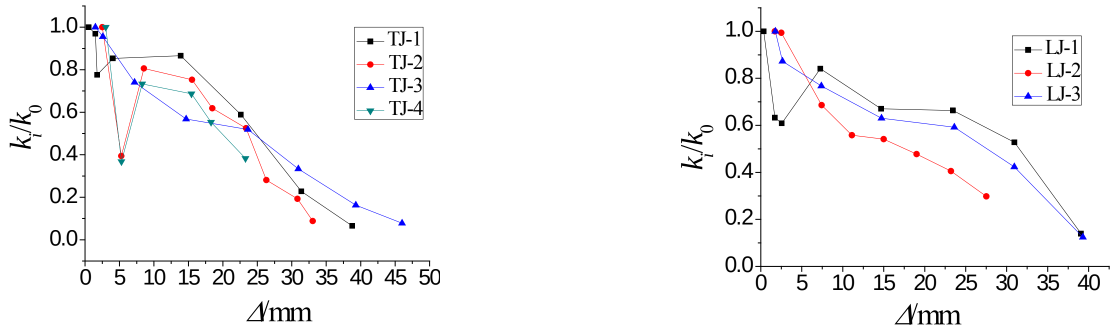

(a) Joint of T-shaped (b) Joint of T-shaped

Fig. 23 Stiffness degradation curves of specimens

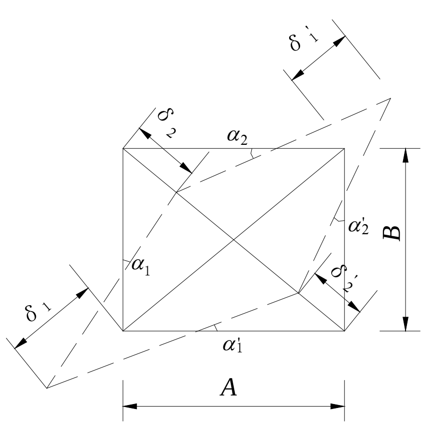

Fig. 24 Shear deformation on core region

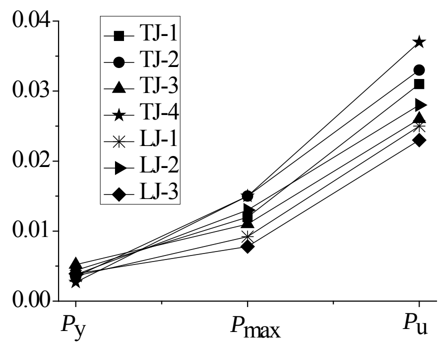

Fig. 25 Shear deformation angle in different stages

Where $+\Delta_i$ and $-\Delta_i$ are the maximum value of the first cycle in both two cyclic directions; $+P_i$ and $-P_i$ are the corresponding loads.

Fig. 23 indicates the stiffness degradation of specimens with L-shaped section and T-shaped section respectively, while initial loop stiffness is defined as K_0. For specimens TJ-2, TJ-4 and LJ-1, there were small clearance between the specimens and loading devices. At the loading stage when $\Delta = 2$ mm and $\Delta = 4$ mm, the clearance led to the evident change on the stiffness degradation curves. Conclusions can be made that with the increase of lateral displacement, stiffness gradually degenerates and becomes more serious when getting the yield displacement. In the same displacement level, increase of axial compression ratio leads to the degeneration of stiffness.

4.7 Deformation

Total story drift Δ is calculated by Eq. (15)

$$\Delta = \Delta_{bc} + \Delta_{pz} \tag{15}$$

Where Δ_{bc} is the story drift caused by bending and shear deformation. Δ_{pz} is the story drift caused by joint shear deformation.

Shear deformation was caused by horizontal shear in joint (Braconi *et al*. 2010), which transformed the shape from rectangular to diamond as shown in Fig. 24. At shear failure point, specimens were in elastic or initial elastic-plastic stage so that bending and shear deformation were relatively small.

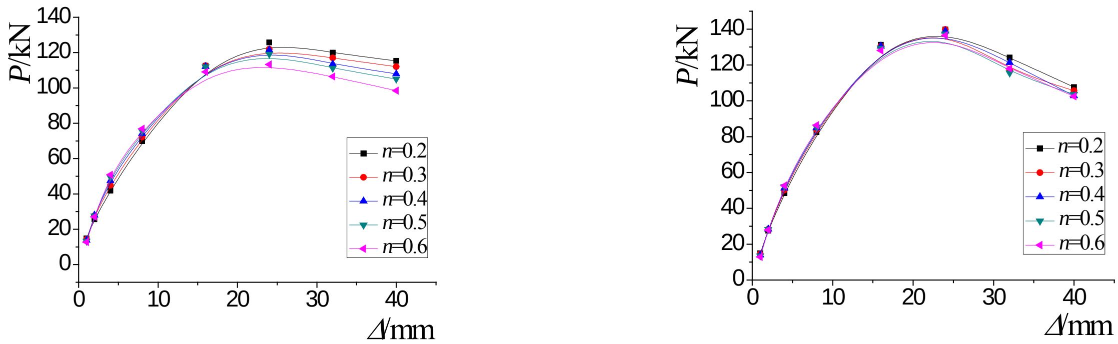

(a) Joint of T-shaped (b) Joint of L-shaped

Fig. 26 Skeleton curves with different axial compression ratio

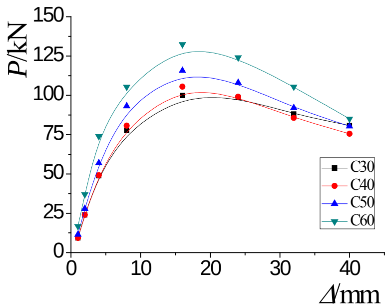

(a) Joint of T-shaped

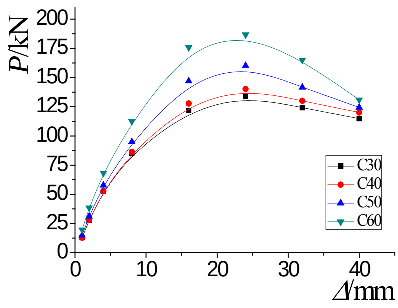

(b) Joint of L-shaped

Fig. 27 Skeleton curves with different concrete grade

Shear deformation angle is measured by electron displacement meters as calculated by Eq. (16)

$$\gamma = \alpha_1 + \alpha_2 = \frac{2ab}{\sqrt{a^2 + b^2}} \left(\delta_1 + \delta_1' + \delta_2 + \delta_2' \right) \tag{16}$$

Where δ_1, δ_1', δ_2, δ_2' are measured displacements.

Shear deformation angles of joint at different stages are given in Fig. 25. At yielding and limiting point, the proportion of shear deformation accounting for total deformation is 20% and 45%, respectively. At failure point, shear deformation angle rapidly increases to 0.025-0.030 rad. Specimens with shear diagonal compression failure had greater shear deformation angles than that of core zone welding crack failure.

5. Parametric studies on seismic behavior

5.1 Influence of axial compression ratio

Fig. 26 shows the influence of axial compression ratio on the joint. Specimens with T-shaped section and L-shaped section nearly have the same trend. With the increase of axial compression ratio, initial stiffness slowly increases. At yielding point, Curves are linear and rise along straight line. The slope of the rising section is basically unchanged. At limiting point, Stiffness severely degenerates but peak load obviously increases. At failure point, the descending branch becomes steeper and failure load reduces.

5.2 Influence of concrete grade

Fig. 27 shows the influence of concrete strength on the joint. Both joints with T-shaped section and L-shaped section are positively influenced with the increases of concrete strength. At yielding point, specimens have higher initial stiffness and bearing capacity. At failure point, slopes of skeleton curves decrease rapidly and ductility obviously becomes poor.

6. Conclusions

The seismic performance of steel beam to concrete-encased composite column with unsymmetrical steel section joints is investigated and discussed with several parameters (concrete strength, stirrup ratio and axial compression ratio). In addition, a nonlinear finite-element analysis is conducted to simulate their seismic behaviors. Following conclusions can be drawn:

- Under the action of axial load and horizontal cyclic loading, steel beam to concrete-encased composite column with unsymmetrical steel section joints mainly have two failure modes, including shear diagonal compression failure and core zone welding crack failure. The failure mode is mainly determined by axial compression ratio. Shear diagonal compression failure occurs in specimens with n = 0.6, and core zone welding crack failure occurs in specimens with n = 0.3.
- Steel beam to concrete-encased composite column with unsymmetrical steel section joints exhibit good energy dissipation capacity and ductility. The displacement ductility coefficients of specimens are about 2.7-3.4. At failure point, column-to-beam rotations are 0.023-0.037. Inter-story drifts are 1/92-1/53. Equivalent viscous coefficients are 0.191-0.268. The structural lateral displacement is caused by the shear deformation in core region, accounting for a large percentage of total horizontal displacement.
- Both increase of axial compression ratio and concrete strength can increase the ultimate bearing capacity, On the other hand ductility and energy absorption capacity degenerate seriously. The ultimate bearing capacity increases for about 15.95% but ductility degenerates for about 12.50% (comparing with TJ-1 and TJ-2,). Increase of stirrup ratio can provide effective constraint on concrete and longitudinal bars, which will increase the deformation capacity and ductility for about 15.18% (comparing with LJ-1 and LJ-3).

A three-dimensional nonlinear finite-element analysis is developed. Material properties (encased steel, concrete and reinforcing bars) and bonding performance between steel skeleton and concrete are carefully considered in model. Finite element analysis effectively simulates the behavior of specimens which are experimentally investigated. The results show that both axial compression ratio and concrete strength have great effect on specimens and are generally consistent with test results. It is possible to accurately predict the cyclic load response of specimens.

Acknowledgments

This research was funded by Natural Science Foundation of Hubei Province of China (Grant No. 2016CFB604), Natural Science Foundation of China (Grant No. 51108041, 51378077), Science Foundation of the Education Department of Hubei Province of China (Grant No. D20161305) and their support are gratefully acknowledged.

References

Abbas, A.A., Mohsin, S.M.S. and Cotsovos, D.M. (2014), "Seismic response of steel fibre reinforced concrete beam-column joints", *Eng. Struct.*, **59**(2), 261-283.

Braconi, A., Elamary, A. and Salvatore, W. (2010), "Seismic behaviour of beam-to-column partial-strength joints for steel-concrete composite frames", *J. Construct. Steel Res.*, **66**(12), 1431-1444.

Chen, Q.J., Cai, J., Mark, A.B., Liu, X.P. and Zuo, Z.L. (2014), "Seismic behaviour of a through-beam connection between concrete-filled steel tubular columns and reinforced concrete beams", *Eng. Struct.*, **80**, 24-39.

Central Research Institute of Building and Construction (2006), *Technical Specification of Steel-reinforced Concrete Structures*. Metallurgical Industry Press, Beijing, China.

Cheng, W., Swaddiwudhipong, S. and Jiang, D. (2003), "Steel-reinforced concrete joints under reversal cyclic load", *Magazine of Concrete Research*, **55**(6), 525-535.

Chidambaram, R.S. and Agarwal, P. (2015), "Seismic behavior of hybrid fiber reinforced cementitious composite beam-column joints", *Mater. Des.*, **86**, 771-781.

China Academy of Building Research (2010a), *Code for Design of Concrete Structures*, China Architecture & Building Press, Beijing, China.

China Academy of Building Research (2010b), *Technical Specification for Steel Reinforced Concrete Composite Structures*, China Architecture & Building Press, Beijing, China.

Choi, S.M., Park, S.H. and Yun, Y.S. (2010), "A study on the seismic performance of concrete-filled square steel tube column-to-beam connections reinforced with asymmetric lower diaphragms", *Steel Construct.*, **66**(7), 962-970.

Constanze, R., Saptarshi, S., Balthasar, N. and Ramanjaneyulu, K. (2015), "Numerical simulation for seismic performance evaluation of fibre reinforced concrete beam–column sub-assemblages", *Eng. Struct.*, **91**, 182-196.

Enrico, S. and Sherif, E. (2004), "Nonlinear analysis of steel-concrete composite structures: State of the art", *J. Struct. Eng.*, **130**(2), 159-168.

Kovács, N., Calado, L. and Dunai, L. (2008), "Experimental and analytical studies on the cyclic behavior of end-plate joints of composite structural elements", *J. Construct. Steel Res.*, **64**(2), 202-213.

Ky, V.S., Tangaramvong, S. and Thepchatri, T. (2015), "Inelastic analysis for the post-collapse behavior of concrete encased steel composite columns under axial compression", *Steel Compos. Struct., Int. J.*, **19**(5), 1237-1258.

Li, J.H., Li, Y.S., Wang, J.M., Wang, X.T. and Xue, J.Y. (2010), "Bond-slip constitutive relation and bond-slip resilience model of shape-steel reinforced concrete columns", *China Civil Eng. J.*, **43**(3), 46-52.

Metelli, G., Messali, F., Beschi, C. and Riva, P. (2015), "A model for beam–column corner joints of existing RC frame subjected to cyclic loading", *Eng. Struct.*, **89**(C), 79-92.

Pantelides, C.P., Okahashi, Y. and Reaveley, L.D. (2008), "Seismic rehabilitation of reinforced concrete frame interior beam-column joints with FRP composites", *J. Compos. Construct.*, **12**(4), 435-445.

Shafaei, J., Hosseini, A. and Marefat, M.S. (2014), "Seismic retrofit of external RC beam-column joints by joint enlargement using prestressed steel angles", *Eng. Struct.*, **81**(81), 265-288.

Vasdravellis, G., Valente, M. and Castiglioni, C.A. (2009), "Behavior of exterior partial-strength composite beam-to-column connections: Experimental study and numerical simulations", *J. Construct. Steel Res.*, **65**(1), 23-35.

Wang, X.M. and Li, Y.Q. (2011), *Analysis and Application of Structure in ANSYS*, China Communications Press, Beijing, China.

Xu, C.H., Zeng, L., Zhou, Q., Tu, X. and Wu, Y. (2015), "Cyclic performance of concrete-encased composite columns with T-shaped steel sections", *Int. J. Civil Eng.*, **13**(4), 456-467.

Xue, J.Y., Liu, Y., Zhao, H.T. and Chen, Z.P. (2011), "Experimental study of the bearing capacity of steel reinforced concrete specially-shaped column-beam joint", *China Civil Eng. J.*, **44**(5), 41-48.

Yu, J.T., Lu, Z.D. and Zhang, K.C. (2010), "Experimental study on seismic behavior of strengthened RC column-beam joints damaged by simulated earthquake", *J. Build. Struct.*, **31**(12), 64-73.

Zeng, L., Xu, C.X., Zheng, S.S. and Lv, Y. (2010), "Nonlinear finite element analysis on SRHSHPC frame joints", *Earthq. Resist. Eng. Retrofit.*, **32**(2), 37-41.

Zeng, P., Lei, L.P. and Fang, G. (2011), *Finite Element Analysis Guide: Modeling and ANSYS of Structure*, Machinery Industry Press, Beijing, China.

Zeng, L, Cui, Z.K., Xiao, Y.F., Jin, S.Q. and Wu, Y.Y. (2015a), "Cyclical behavior of concrete-encased composite frame joints with high strength concrete", *Adv. Mater. Sci. Eng.*, **6**, 1-13.

Zeng, L., Parvasi, S.M., Kong, Q.Z., Huo, L.S., Lim, L., Li, M. and Song, G.B. (2015b), "Bond slip detection of concrete-encased composite structure using shear wave based active sensing approach", *Smart Mater. Struct.*, **67**(2), 211-222.

Zhang, D.C., Guo, Y. and Li, B.H. (2013), "Experimental studies on aseismic performance of T-shape fabricated concrete joints with precast external shell and cast-in-place core concrete", *Eng. Mech.*, **30**(1), 156-162.

Zhen, S.S., Zeng, L., Lv, Y., Sun, Q.G. and Wang, P.Q. (2008), "Experimental research on seismic behavior of steel rei nforced high strength and high performance concrete frame joints", *J. Build. Struct.*, **29**(3), 128-136.

Zheng, S.S. and Zeng, L. (2008), "Experimental research on seismic behavior of steel reinforced highstrength and high performance concrete frame joints", *J. Build. Struct.*, **29**(3), 74-81.

Zhou, T., Chen, Z.H. and Liu, H.B. (2012), "Seismic behavior of special shaped column composed of concretefilled steel tubes", *J. Struct. Eng.*, **75**(7), 131-141.

Zhou, T., Jia, Y., Xu, M., Wang, X.D. and Chen, Z.H. (2015), "Experimental study on the seismic performance of L-shaped column composed of concrete-filled steel tubes frame structures", *J. Construct. Steel Res.*, **114**, 77-88.

CC